

Simulation of fine-scale electrical conductivity fields using resolution-limited tomograms and area-to-point kriging

Raphaël Nussbaumer¹, Niklas Linde¹, Grégoire Mariethoz² and Klaus Holliger^{1,3}

¹Institute of Earth Sciences, University of Lausanne, CH-1015 Lausanne, Switzerland. E-mail: raphael.nussbaumer@unil.ch

²Institute of Earth Surface Dynamics, University of Lausanne, CH-1015 Lausanne, Switzerland

³School of Earth Sciences, Zhejiang University, 310027 Hangzhou, China

Accepted 2019 April 18. Received 2019 April 1; in original form 2018 February 21

SUMMARY

Deterministic geophysical inversion approaches yield tomographic images with strong imprints of the regularization terms required to solve otherwise ill-posed inverse problems. While such tomograms enable an adequate assessment of the larger-scale features of the probed subsurface, the finer-scale details tend to be unresolved. Yet, representing these fine-scale structural details is generally desirable and for some applications even mandatory. To address this problem, we have developed a two-step methodology based on area-to-point kriging to generate fine-scale multi-Gaussian realizations from smooth tomographic images. Specifically, we use a co-kriging system in which the smooth, low-resolution tomogram is related to the fine-scale heterogeneity through a linear mapping operation. This mapping is based on the model resolution and the posterior covariance matrices computed using a linearization around the final tomographic model. This, in turn, allows us for analytical computations of covariance and cross-covariance models. The methodology is tested on a heterogeneous synthetic 2-D distribution of electrical conductivity that is probed with a surface-based electrical resistivity tomography (ERT) survey. The results demonstrate the ability of this technique to reproduce a known geostatistical model characterizing the fine-scale structure, while simultaneously preserving the large-scale structures identified by the smoothness-constrained tomographic inversion. Small discrepancies between the geophysical forward responses of the realizations and the reference synthetic data are attributed to the underlying linearization. Overall, the method provides an effective and fast alternative to more comprehensive, but computationally more expensive approaches, such as, for example, Markov chain Monte Carlo techniques. Moreover, the proposed method can be used to generate fine-scale multivariate Gaussian realizations from virtually any smoothness-constrained inversion results given the corresponding resolution and posterior covariance matrices.

Key words: Electrical resistivity tomography (ERT); Inverse theory; Spatial analysis; Statistical methods; Tomography.

1 INTRODUCTION

Most geophysical inversions are formulated as deterministic smoothness-constrained problems in which solutions are sought that maximize the regularization weight under the constraint that the observations are fitted to a pre-defined noise level (e.g. DeGroot-Hedlin & Constable 1990). In such approaches, the subsurface is discretized with cells that are much finer than the resolution of the resulting tomographic images. An advantage of this inherent over-parametrization is that the resolved features in the tomograms are essentially independent of the model parametrization. For example, in the case of electrical resistivity tomography (ERT), which relies on multiple, partially overlapping surface- and/or borehole-based

measurements of electrical resistances to infer the electrical resistivity distribution of the probed subsurface region, a smoothness-constraining regularization term ensures uniqueness of an otherwise ill-posed problem (e.g. Binley & Kemna 2005). However, this comes at the cost of tomographic images that only retain the larger-scale structures that are resolved by the data.

The absence of the finer-scale heterogeneity can be problematic, notably in the context of aquifer and reservoir characterization where resolution-limited tomographic images of geophysical properties are commonly used to extrapolate point-type measurements of the hydraulic target properties (e.g. Rubin *et al.* 1992; Carty *et al.* 1993; Hubbard *et al.* 2001). Unfortunately, using upscaled geophysical information from tomograms in such procedures will

lead to severe bias (Day-Lewis & Lane 2004; Moysey *et al.* 2005). Accounting for small-scale fluctuations in hydraulic conductivity is indeed essential to appropriately describe transport and mixing processes (e.g. Dentz *et al.* 2011). In this context, geostatistical methods can be helpful to impose small-scale properties on the solution under the assumption of a known underlying covariance model.

There are two general approaches to reproduce fine-scale structure in geophysical images: modifying the inverse problem or applying downscaling methods *a posteriori*. The first and, arguably, most generic approach is to replace the deterministic smoothness-constrained solution and find alternative methods that directly account for the geostatistical model of interest. In the case of a linear forward problem, the Gaussian linear inverse theory (Hansen *et al.* 2006) can be used to derive the mean model and the covariance of the model parameters. This estimate is closely related to the co-kriging estimate (Gloaguen *et al.* 2005; Gloaguen *et al.* 2007). Simulations can then be generated with the Gaussian error simulation (Journel & Huijbregts 1978; Gloaguen *et al.* 2004) or sequential simulation (Hansen & Mosegaard 2008). In the case of nonlinear problems, a probabilistic formulation of the inverse problem can be used to generate an ensemble of model realizations that collectively characterize a posterior probability density function (pdf). By relying on advanced global search strategies, such as, for example, Markov chain Monte Carlo (MCMC) algorithms, it is possible to consider very generic classes of geostatistical models (e.g. Ramirez *et al.* 2005; Hansen *et al.* 2012; Linde *et al.* 2015b). The associated computational costs do, however, tend to be very high. Using a least-squares measure of data fit and assuming a stationary multi-Gaussian prior, it is possible to solve a nonlinear optimization problem based on iterative linearization, which is reminiscent of classical deterministic inversion, albeit with a solution that enables multiple model realizations to be obtained that are consistent with a geostatistical covariance model (Tarantola & Valette 1982; Kitanidis 1995; Yeh *et al.* 2002; Englert *et al.* 2016). Here, a covariance model essentially replaces the regularization term (e.g. Linde *et al.* 2006) and the regularization weight is unity. This technique is widely used for addressing hydraulic inverse problems (Kitanidis & Vomvoris 1983; Hoeksema & Kitanidis 1984; Li *et al.* 2005), but is seldom considered in geophysical inversion methods, which generally rely on smoothness-constrained or related deterministic techniques.

The second approach is to downscale the tomogram resulting from the deterministic smoothness-constrained inversion, based on some ad hoc method or, more commonly, to directly simulate the property of interest as a primary variable and using the tomogram as a secondary variable. For example, McKenna & Poeter (1995) and Cassiani *et al.* (1998) use seismic tomograms as secondary variables in co-kriging systems to estimate the hydraulic conductivity and hydrofacies, respectively. These approaches involve fitting variograms and cross-variograms to known hard data. Doyen & Boer (1996) and Chen *et al.* (2001) do not fit a cross-variogram model, but instead, construct a joint pdf of the primary and secondary variables with collocated hard data. During the simulation of the primary variable, the kriging estimation is updated with the joint pdf sampled conditionally to the known collocated secondary variable. However, the difference in resolution between the primary and secondary variables is not explicitly taken into account in these studies. Ruggeri *et al.* (2013a, 2014) use a two-step approach to first downscale an ERT image and then use the resulting fine-scale information to simulate stochastically the associated small-scale distribution of the hydraulic conductivity. This approach does, however, suffer from

an inability to accurately account for the conditional dependence of information (Mariethoz *et al.* 2009). The basic underlying problem is that the model estimates of the tomograms are treated as independent data, while the number of degrees of freedom is much smaller than the number of model parameters. The impact of this loss of resolution inherent to smoothness-constrained inversions has been extensively studied in the hydrogeophysics literature, thereby highlighting the need to properly account for this phenomenon when inferring hydraulic properties or state variables (Day-Lewis & Lane 2004; Moysey & Knight 2004; Moysey *et al.* 2005; Singha *et al.* 2007).

Our study focuses on the second two-step approach with the geophysical inversion being performed using smoothness constraints. It is undeniable that a more appropriate and elegant way would be to reformulate the geophysical inversion using regularization term based on the assumed geostatistical model. However, since most commercial or academic geophysical inversion software only provide regularizations in terms of smoothness or damping constraints, the second approach becomes essential if the output of such codes is to be used in a multi-Gaussian framework. In addition, this approach allows the inversion to be performed on a much coarser grid, thus, reducing the computational burden. In the geostatistical community, several methods exist for downscaling a geostatistical variable. This is known as the change of support problem (Gotway & Young 2002; Atkinson 2013). Among these methods, area-to-point kriging (Kyriakidis 2004) is an adapted co-kriging technique for the particular case when the known secondary variable is an upscaled description of the unknown primary variable. Kyriakidis (2004) shows that the area-to-point estimator is unbiased and has minimum error variance. Furthermore, it is a coherent estimation, that is, upscaling the area-to-point estimation of the primary variable reproduces the secondary variable. Kyriakidis & Yoo (2005) extended this method to generate stochastic realizations through Gaussian error simulation.

However, in order to use area-to-point kriging to downscale the tomogram, a linear relationship between the target fine-scale realization and the large-scale and smooth tomogram needs to be quantified. A key idea of our methodology is to use traditional image appraisal tools from linear geophysical tomography to build this linear relationship. More specifically, (i) the model resolution matrix, which describes the averaging filter relating the resulting tomographic image to the ‘true’ subsurface structure, and (ii) the posterior model covariance matrix, which quantifies the influence of data errors on parameter errors (e.g. Menke 1989; Friedel 2003). For the nonlinear case, the same theoretical framework can be readily applied through a local uncertainty assessment by linearizing the problem around the final model (Alumbaugh & Newman 2000).

In this work, we describe a methodology to generate stochastic fine-scale realizations of electrical conductivity based on deterministic smoothness-constrained ERT images using area-to-point kriging. In doing so, we account for the averaging process inherent to the deterministic smoothness-constrained iterative inversion process by incorporating the information from the resolution and posterior model covariance matrices. We focus on electrical conductivity because of the high importance of this rock physical property and of ERT-based imaging for a wide variety of important applications. It is, however, important to note that the methodological framework can be readily applied to any other smoothness-constrained geophysical inverse problem.

The paper is structured as follows. In Section 2, the methodological background is presented by introducing smoothness-constrained

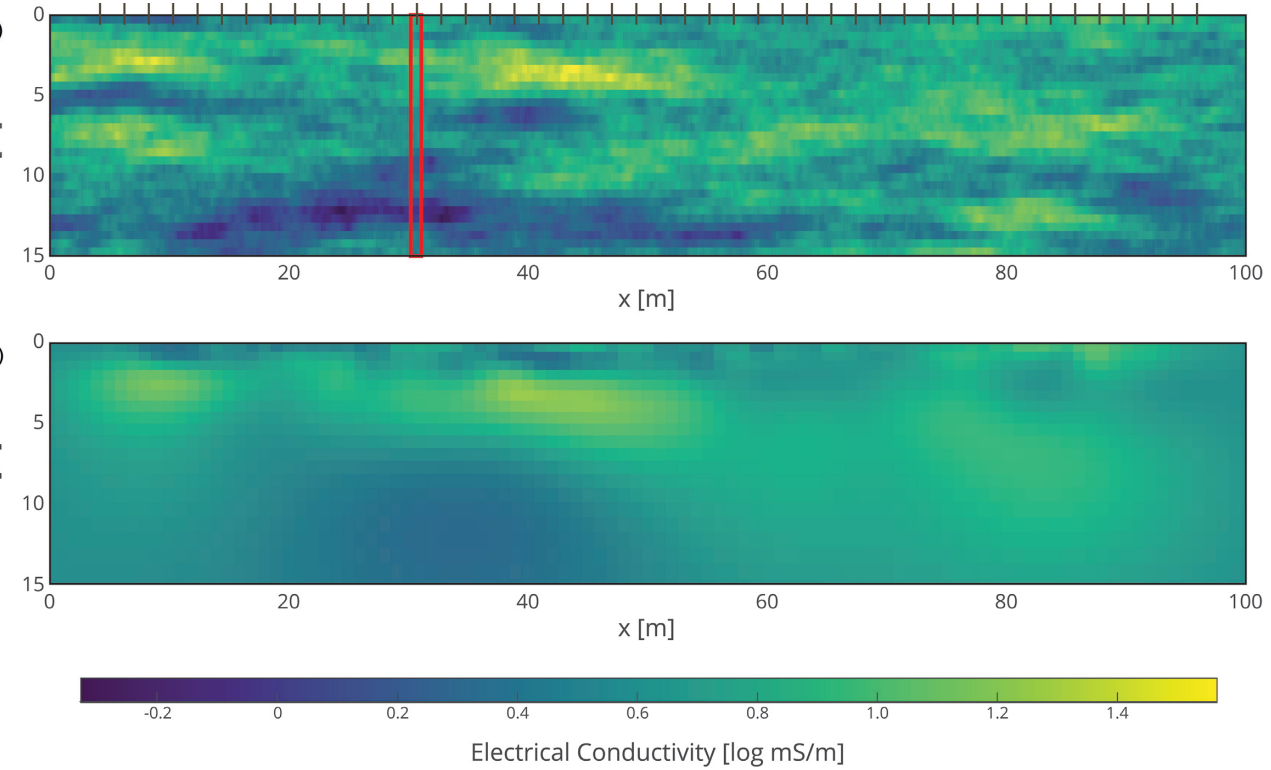


Figure 1. (a) True fine-scale electrical conductivity field σ^{true} and (b) corresponding surface-based ERT estimate Σ^{est} . The red rectangle denotes the location of a borehole, along which the true electrical conductivity is known. The brown vertical line segments in (a) indicate the locations of the 47 electrodes used. The tomogram (b) resulting from deterministic inversion shows the typical loss of fine-scale structure, increasing with depth but with the general structure still visible. The aim of the present method is to retrieve stochastic fine-scale realizations from this estimate and local borehole information.

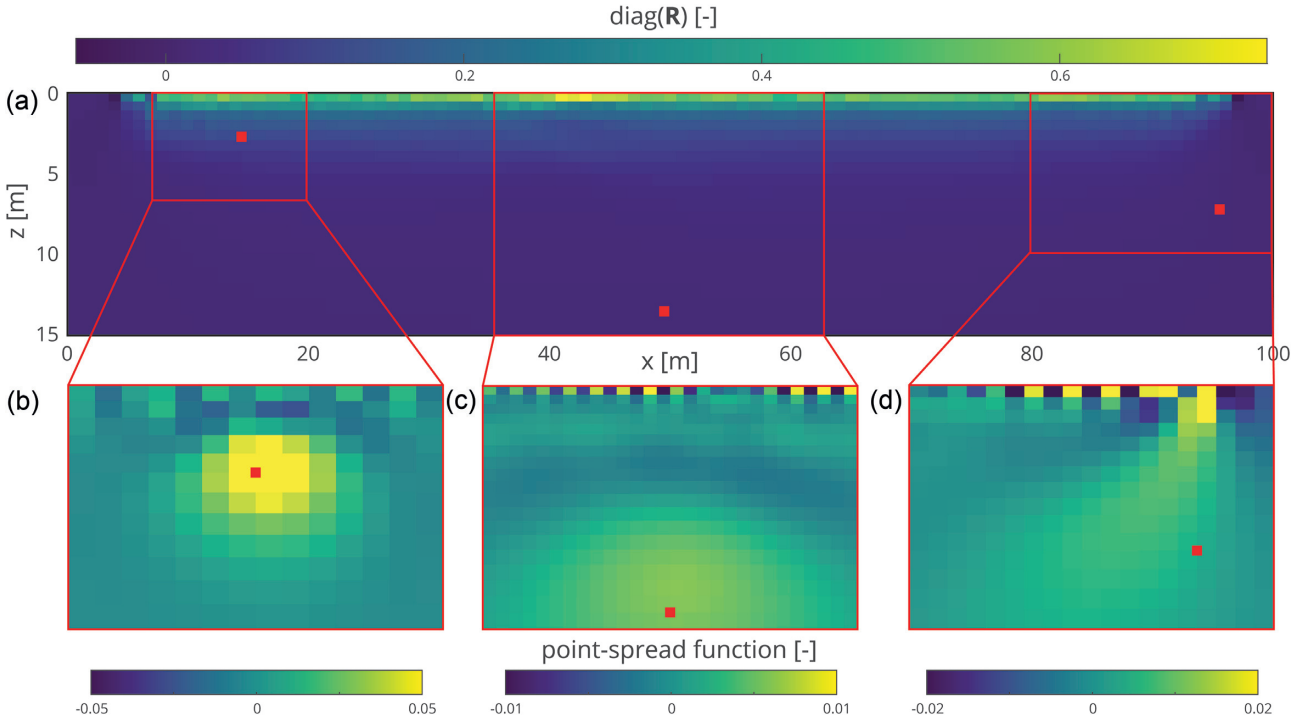


Figure 2. (a) Diagonal of the resolution matrix reshaped into a 2-D grid. (b-d) Rows of the resolution matrix (point-spread functions) corresponding to the locations denoted by the red dots in the zoomed subfigures. Note that different colour scales are used in each panel in order to highlight the characteristic features. The values of the resolution matrix quantify the smoothing resulting from the inversion. Thus, the sum of rows is equal to 1. A higher value implies a stronger influence of the corresponding true value for the estimate.

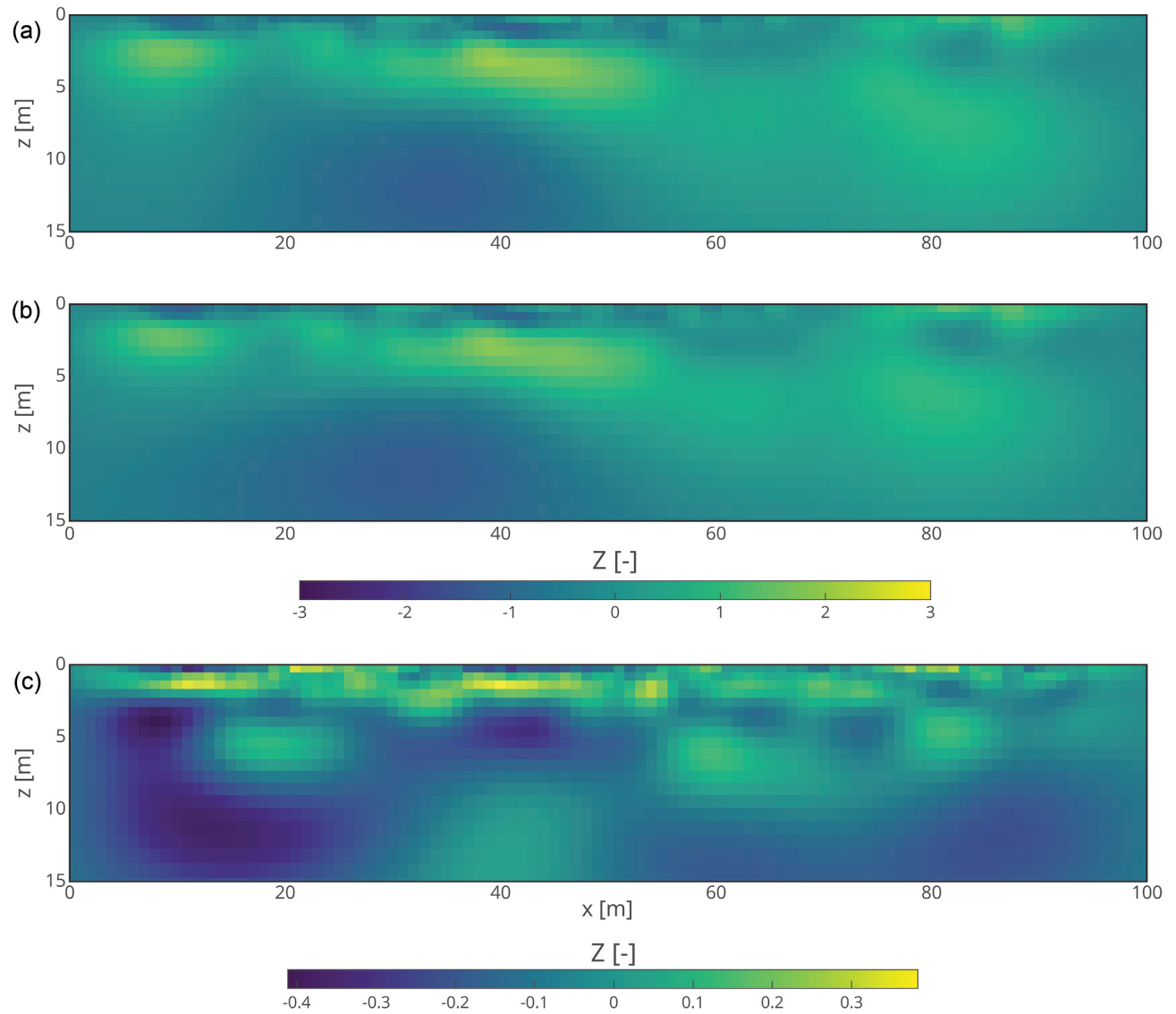


Figure 3. (a) Σ^{est} resulting from the tomographic inversion, (b) RU-transform of the true field $R U z^{\text{true}}$ and (c) difference between the two. The small error between the two demonstrates the ability of the RU-transform to account for the upscaling and smoothing.

geophysical inversion and area-to-point kriging followed by an elaboration of how to combine them. Section 3 then presents the testing and assessment of the proposed technique with regard to a pertinent synthetic case study.

2 METHODOLOGY

2.1 Problem set-up

Consider a true synthetic fine-scale heterogeneous electrical conductivity field σ^{true} (Fig. 1a) and the corresponding estimation on a coarser grid (details follow later) of a deterministic smoothness-constrained ERT-type inversion Σ^{est} (Fig. 1b). Comparing Figs 1(a) and (b) illustrates the generally lower and spatially variable resolution of the ERT image. Notably, the systematic decrease of the model resolution with depth is clearly evident. Retrieving the underlying fine-scale structure from such a tomogram, which can be regarded as representing upscaled information with a spatially variable support, is an inherently non-unique problem. Indeed, this particular smooth

upscaled representation of the underlying electrical conductivity structure could have arisen from a wide variety of fine-scale structures. This is the example that we will consider throughout this study.

The aim of our method is to generate fine-scale electrical conductivity simulation σ^{sim} constrained to the smooth and coarser ERT image Σ^{est} based on the knowledge of an underlying geostatistical model. In addition, we consider local in situ measurements σ^{hd} as additional constraints, denoted by a red line in Fig. 1(a).

Both variables σ^{true} and Σ^{est} are in logarithmic scale because the electrical conductivity is assumed log-normally distributed and it is, therefore, common practice to perform ERT inversions in logarithmic scale.

In the following, uppercase characters are used when referring to variables defined on the grid with coarse resolution (on which inversions are carried out), while lowercase characters are used for variables existing on the grid with fine resolution (on which geostatistical simulation is carried out). For instance, Σ^{est} belongs to the coarser grid, while σ^{true} is defined on the fine-resolution grid.

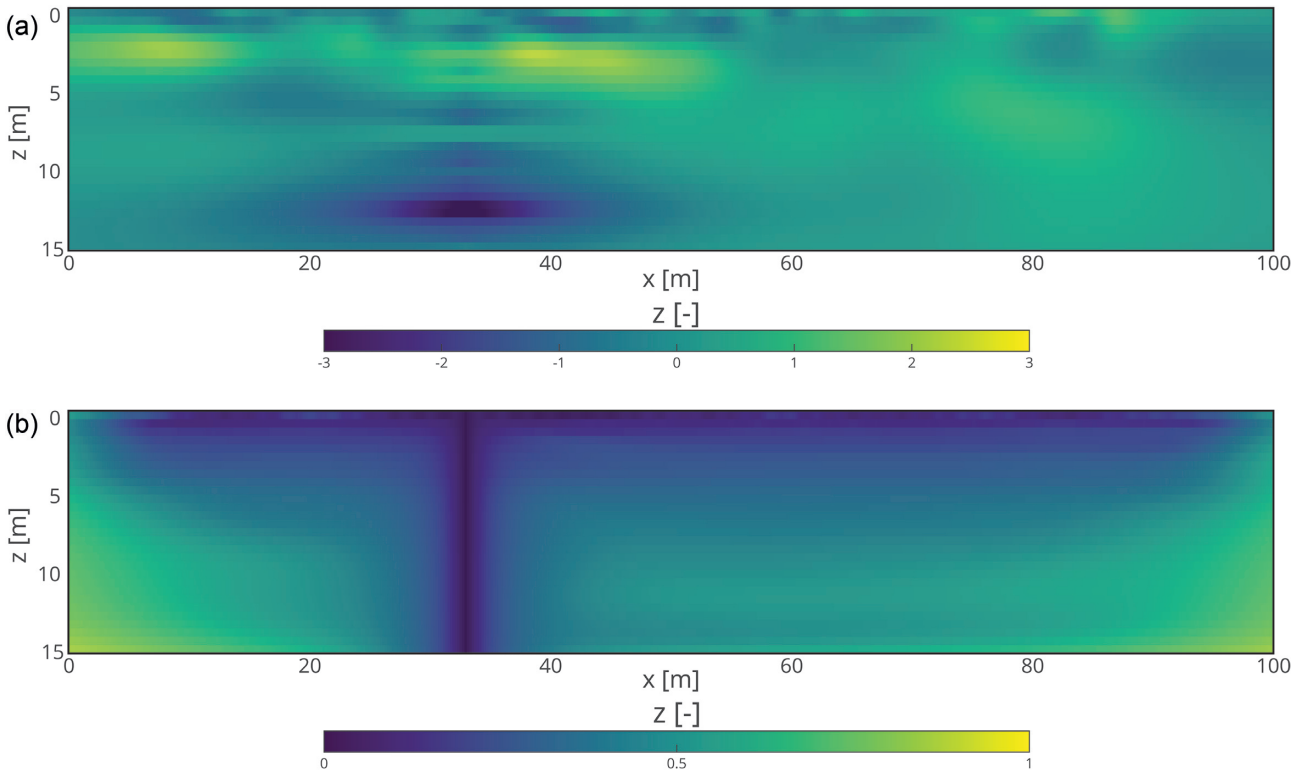


Figure 4. (a) Area-to-point kriging estimation based on the tomographic image and the hard data $\hat{\mathbf{z}} = \mathbf{A}_{\text{hd}} \mathbf{z}^{\text{hd}} + \mathbf{A} \mathbf{Z}^{\text{est}}$ and (b) corresponding kriging error variance (e.g. Kyriakidis 2004). Compared to the tomographic inversion, the gain is the variance at each cell (informing about the uncertainty of the estimate) and the covariance structure informing about the spatial relation among these cells under the assumption of a known geostatistical model.

In addition, bold symbols denote vectors or matrices. Note that the grid size does not need to be constant, thus allowing to use a coarse grid with larger cell sizes with depth as typically used in surface-based ERT inversion. The linear operator \mathbf{U} performs the upscaling from the fine-resolution to the coarse resolution grid

$$\boldsymbol{\Sigma} = \mathbf{U} \boldsymbol{\sigma}. \quad (1)$$

In practice, \mathbf{U} is constructed with a gridded linear 2-D interpolation, where $\mathbf{U}(i, j)$ is the weight of $\boldsymbol{\sigma}(j)$ in defining the average $\boldsymbol{\Sigma}(i)$, such that the sum of each row is equal to one.

2.2 Geophysical inversion and model appraisal

A forward model $f()$ is used to simulate the response of a given electrical conductivity distribution in terms of the electrical resistances \mathbf{r}^{obs} that would be measured with the electrodes located on the surface. The inversion procedure takes such data to estimate the distribution of the electrical conductivity $\boldsymbol{\Sigma}^{\text{est}}$ throughout the probed subsurface. Inverse problems of this type tend to be ill-posed and, hence, are typically solved with a regularized least-squares optimization of an objective function consisting of the sum of the data misfit and a model regularization term (e.g. Menke 1989; DeGroot-Hedlin & Constable 1990)

$$\Psi(\boldsymbol{\Sigma}) = \|\mathbf{W}_r [\mathbf{r}^{\text{obs}} - f(\boldsymbol{\Sigma})]\|_2^2 + \alpha \|\mathbf{W}_\Sigma \boldsymbol{\Sigma}\|_2^2, \quad (2)$$

where \mathbf{W}_r is a data weighting matrix related to the observational errors and their correlations and \mathbf{W}_Σ is the model regularization operator, which is typically the discrete first-order derivative. During

the inversion process, the regularization parameter α is maximized under the constraint that the data are fitted to a predefined error level (Constable *et al.* 1987). Nonlinear inverse problems are solved iteratively based on successive linearization around the model obtained in the previous iteration.

The model resolution matrix \mathbf{R} relates the unknown true coarse model parameters to the estimated parameters

$$\boldsymbol{\Sigma}^{\text{est}} = \mathbf{R} \boldsymbol{\Sigma}^{\text{true}}. \quad (3)$$

It can be approximated based on a linearization around the final model obtained at the last iteration p (Newman & Alumbaugh 2000)

$$\mathbf{R} = (\mathbf{J}_p^T \mathbf{W}_r^T \mathbf{W}_r \mathbf{J}_p + \alpha_p \mathbf{W}_\Sigma^T \mathbf{W}_\Sigma)^{-1} \mathbf{J}_p^T \mathbf{W}_r^T \mathbf{W}_r \mathbf{J}_p, \quad (4)$$

where the sensitivity matrix \mathbf{J}_p is obtained by linearizing $f()$ around the model obtained in the p^{th} iteration. Data errors lead to uncertain estimates and the model regularization imposes a high spatial correlation between the inverted values. These effects are captured by the posterior covariance matrix

$$\mathbf{C}_\Sigma^{\text{est}} = (\mathbf{J}_p^T \mathbf{W}_r^T \mathbf{W}_r \mathbf{J}_p + \alpha_p \mathbf{W}_\Sigma^T \mathbf{W}_\Sigma)^{-1}. \quad (5)$$

Fig. 2(a) displays the diagonal of \mathbf{R} for the present example (details later) reshaped into a 2-D grid, thus, indicating to which degree each cell of the domain is resolved. The pixels in the top row are resolved up to 60–70 per cent. This value decreases with depth and reaches near-zero values at the bottom and at the lateral edges of the domain. Each row of the resolution matrix,

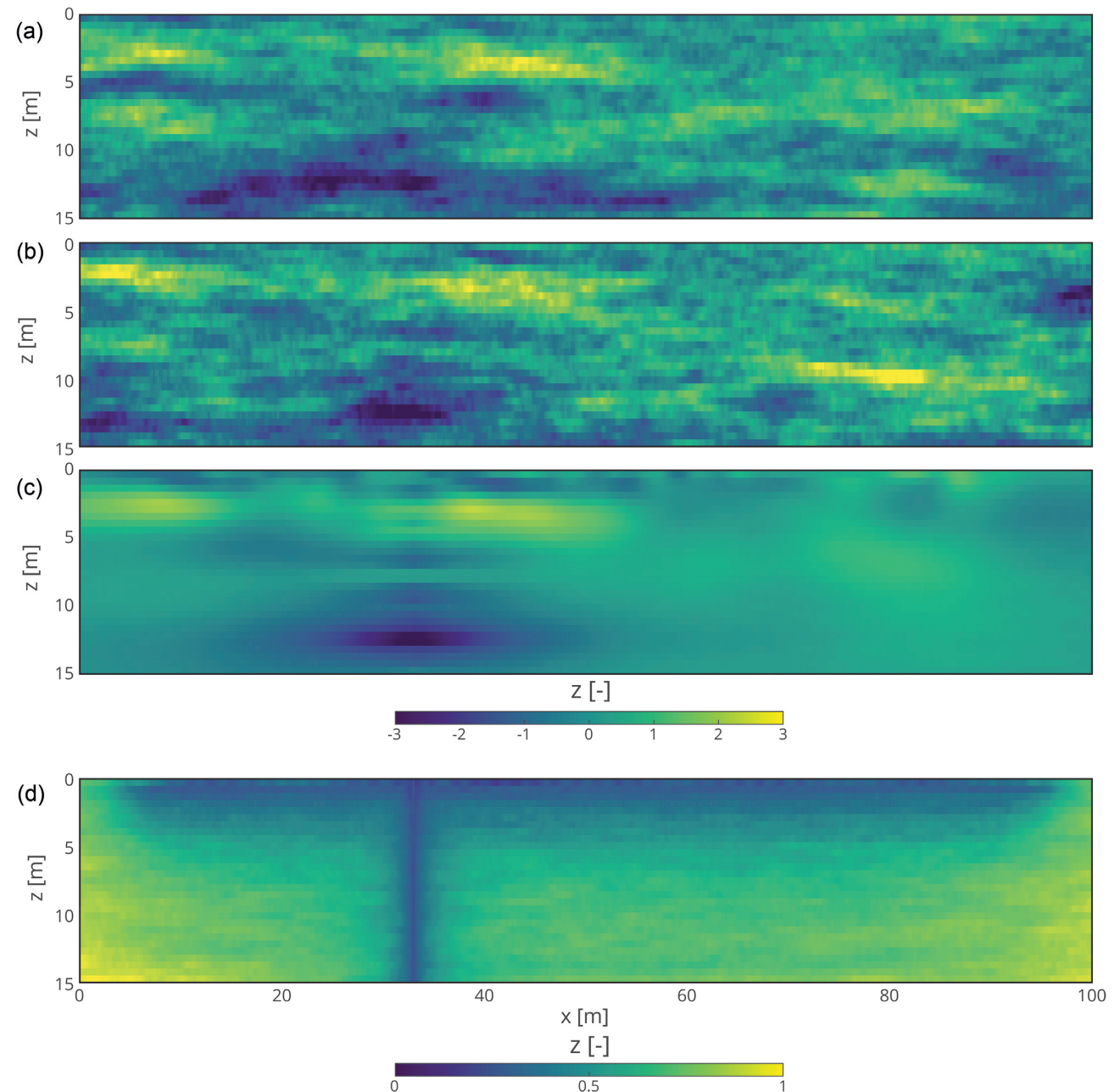


Figure 5. Results of stochastic simulations. (a) True initial field \mathbf{z}^{true} , (b) example of a realization $\mathbf{z}_c^{\text{sim}}$, (c) mean of 500 realizations $\bar{\mathbf{z}}_c^{\text{sim}}$ and (d) standard deviation of the same 500 realizations $\text{std}(\mathbf{z}_c^{\text{sim}})$. The realization (b) shows the ability of the method to retrieve similar fine-scale structure as the true field (a). The empirical mean and variance (c and d) are correctly reproducing the theoretical ones (Figs 6a and b).

also known as the point-spread function, corresponds to the relative spreading of the information associated with a given node over the other nodes, so that $\Sigma^{\text{est}}(i) = \mathbf{R}(i, :) \Sigma^{\text{true}}$. Figs 2(b)–(d) display the point-spread-functions corresponding to three different locations marked with a red dot in Fig. 2(a). Figs 2(b)–(d) only show subdomains of Fig. 2(a), as denoted by red rectangles, because the remaining domain has a relatively limited influence and thus low values. These three examples demonstrate the ability of the resolution matrix to provide information for each individual cell of the grid with regard to the specific averaging pattern imposed by the inversion on each cell. This is exemplified by a small and well-defined radius of influence for

cells located near the surface (Fig. 2b), a larger and more diffuse contribution for deeper cells with values of weights oscillating from positive to negative (Fig. 2c), and an asymmetric shape of influence for cells located near the lateral edges of the domain (Fig. 2d).

2.3 Area-to-point simulation based on ERT tomogram

In this section, it is demonstrated how the kriging estimation and simulation of the fine-scale electrical conductivity σ is achieved using area-to-point kriging. This requires σ to be multi-Gaussian with a known structure $\sigma \sim \mathcal{N}(\mu_\sigma, s_\sigma^2 C_\sigma)$, where μ_σ is the mean

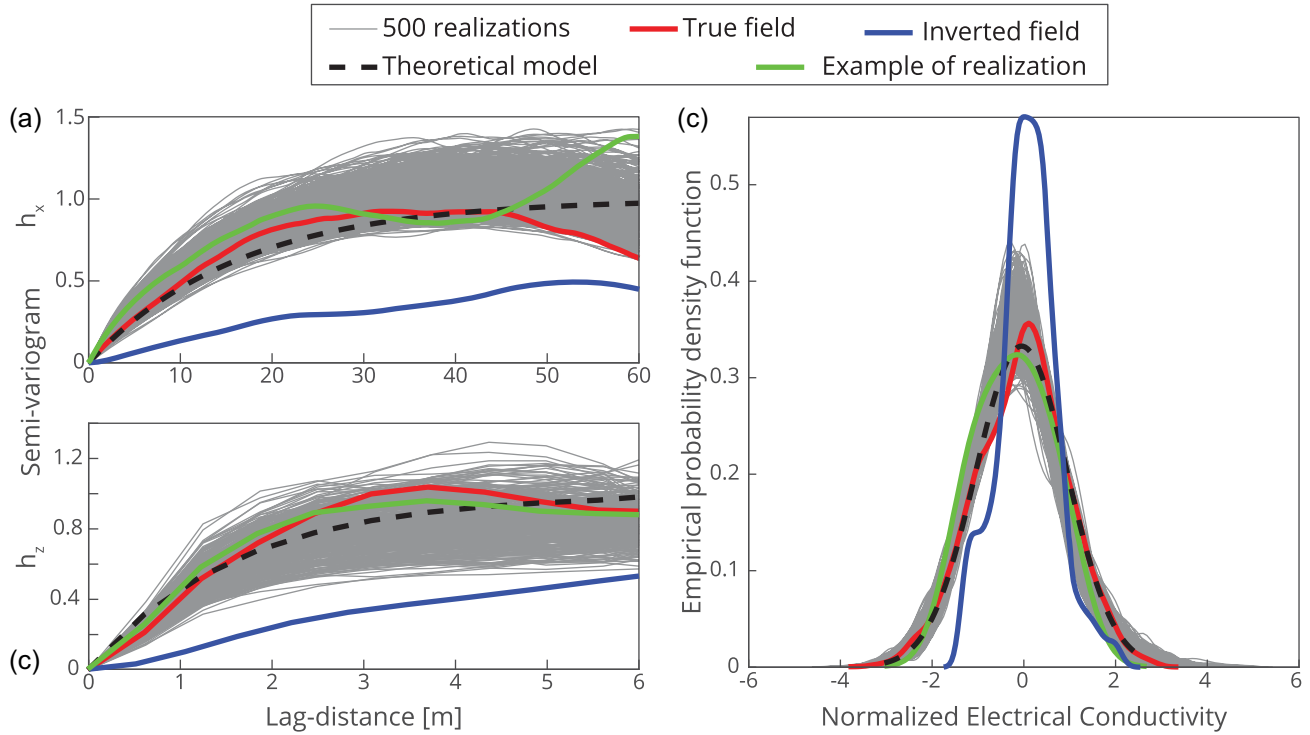


Figure 6. (a) Horizontal and (b) vertical semi-variograms, and (c) probability density function based on 500 realizations (grey lines), example of the individual realization shown in Fig. 5(b) (green line), true field (red line), inverted field (blue line) and theoretical model (dashed black line) superimposed. The good match between the realizations and the theoretical model illustrates the ability of the method to reproduce the two-point statistics. This can also be observed that the ergodic fluctuation for the true field is influencing the realizations with similar deviation from the theoretical model.

vector, s_σ^2 is the variance, and \mathbf{C}_z is the normalized covariance matrix.

Kriging systems are more conveniently expressed with normalized variables. Thus, the electrical conductivity σ and Σ are transformed into their standard normal counterparts,

$$\mathbf{z} = \frac{\sigma - \mu_\sigma}{s_\sigma} \quad (6)$$

and

$$\mathbf{Z} = \frac{\Sigma - \mu_\sigma}{s_\sigma}. \quad (7)$$

The area-to-point kriging estimate $\hat{\mathbf{z}}$ is given by the linear combination of \mathbf{Z}^{est} weighted by the coefficients Λ

$$\hat{\mathbf{z}} = \Lambda \mathbf{Z}^{\text{est}}. \quad (8)$$

In analogy to traditional kriging, the weights Λ are obtained by solving a linear system of equations constructed from the covariance matrix \mathbf{C}_z and the cross-covariance \mathbf{C}_{zZ}

$$\mathbf{C}_z \Lambda = \mathbf{C}_{zZ}. \quad (9)$$

However, solving this linear system of equations requires the computation of \mathbf{C}_z and \mathbf{C}_{zZ} . In the area-to-point kriging framework, they are computed based on upscaling between \mathbf{Z}^{est} and \mathbf{z}^{true} expressed as a linear mapping. In the current framework, this linear mapping can be shown (see Appendix A) to be equal to $\mathbf{R}\mathbf{U}$, thus leading to

$$\mathbf{Z}^{\text{est}} = \mathbf{R}\mathbf{U}\mathbf{z}^{\text{true}}. \quad (10)$$

The strong resemblance between \mathbf{Z}^{est} (Fig. 3a) and $\mathbf{R}\mathbf{U}\mathbf{z}^{\text{true}}$ (Fig. 3b) as well as the comparatively small residuals (Fig. 3c)

demonstrates the ability of the resolution matrix to correctly represent the smoothing effect inherent to the inversion.

Using this linear mapping, the cross-covariance with respect to \mathbf{Z} can be computed as

$$\mathbf{C}_{zZ} = \mathbf{C}_z(\mathbf{R}\mathbf{U})^T, \quad (11)$$

and the covariance matrix of \mathbf{Z} is

$$\mathbf{C}_Z = (\mathbf{R}\mathbf{U}) \mathbf{C}_z(\mathbf{R}\mathbf{U})^T. \quad (12)$$

The covariance \mathbf{C}_Z used in the kriging system (eq. 9) also needs to account for the effects of the data errors and the regularization used in the inversion process. This is detailed in Appendix B.

3 RESULTS

3.1 Synthetic data

In the following, the methodology outlined above is tested for a synthetic case study of a heterogeneous alluvial aquifer for which the field parameters are inspired by those recently reported by Pirot *et al.* (2017). The true fine-scale synthetic electrical conductivity structure (Fig. 1a) is generated using the Fast-Fourier Transform Moving Average (FFT-MA) method (Le Ravalec-Dupin *et al.* 2000) from a log-normally distributed porosity field $\log(\Phi^{\text{true}}) \sim \mathcal{N}(\mu_\phi, s_\phi^2 \mathbf{C}_Z)$ (Pirot *et al.* 2017). Using Archie's law for saturated media (Archie 1942),

$$\sigma(\phi) = \sigma_w \phi^m, \quad (13)$$

this porosity field is transformed into an electrical conductivity field, which thereafter is considered as the true electrical conductivity model. The cementation exponent m and the electrical conductivity

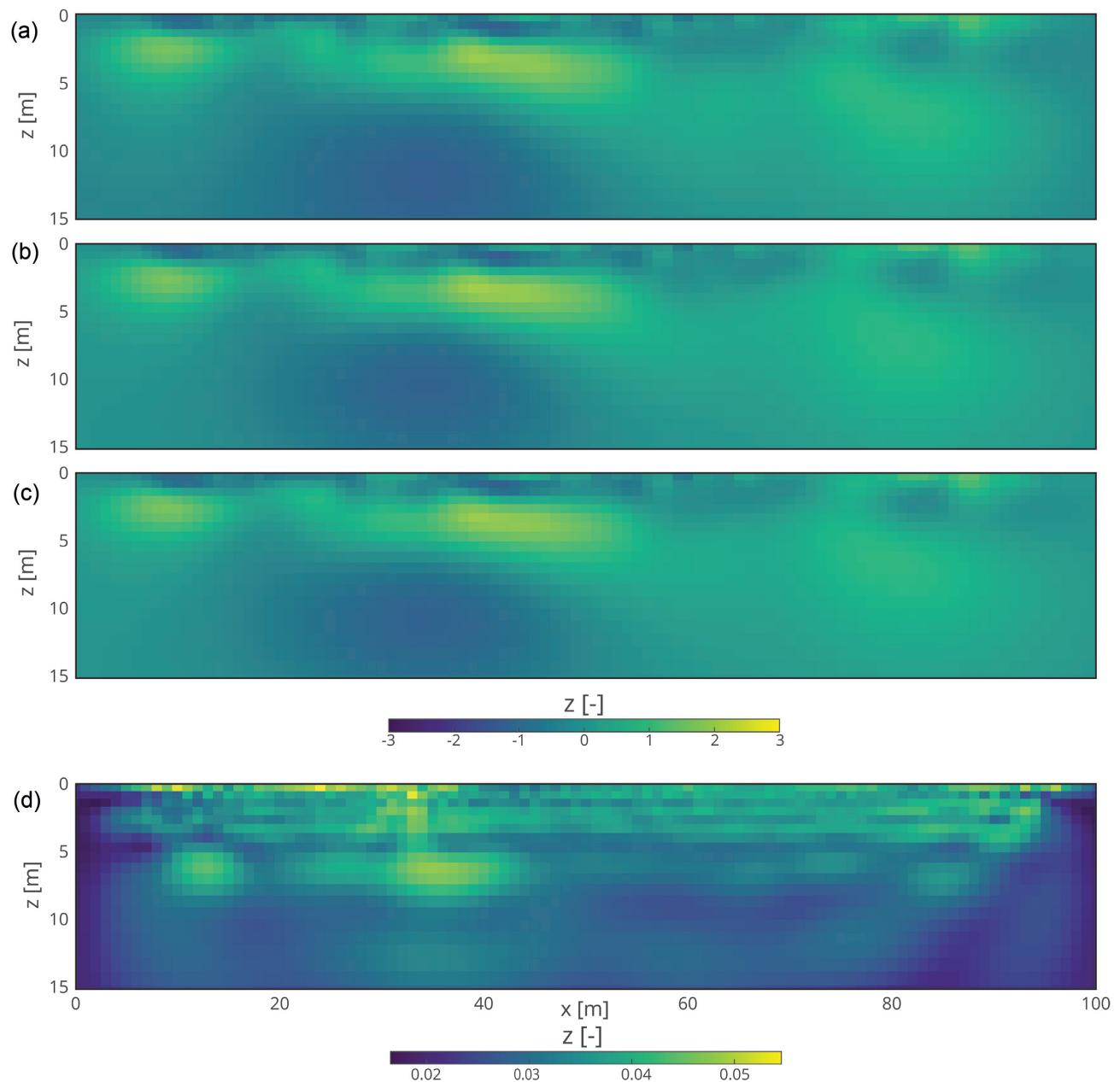


Figure 7. Results of the stochastic simulations. (a) Inverted field, (b) upscaled version or RU-transform of a single example of realizations, (c) mean of the RU-transforms of 500 realizations and (d) standard deviation of the RU-transforms of 500 realizations. The ability of the method to reproduce the tomogram is indicated by the good match between the mean RU-transforms of the realizations and the inverted field (a).

of pore water σ_w are assumed to be known and constant throughout the study area, which is a common approximation for a given hydrogeological unit (e.g. Ruggeri *et al.* 2013, 2014). Consequently, the mean μ_σ and standard deviation s_σ of the electrical conductivity is related to those of the porosity using Archie's law with

$$\mu_\sigma = \log(\sigma_w) + m\mu_\phi \quad (14)$$

and

$$s_\sigma = ms_\phi. \quad (15)$$

On this true fine-scale electrical conductivity field, two types of acquisitions are performed. First, hard data are sampled from a hypothetical borehole located at a lateral distance of 33 m (Fig. 1a).

These data are considered error-free measurements of the electrical conductivity at the resolution of the true field.

Second, the resistances simulated with a surface-based ERT-type geoelectric survey are evaluated using the forward modelling part of the software R2 (Binley & Kemna 2005), which corresponds to a 2.5D solver of the Poisson equation. The boundary conditions along all four boundaries are of the Neumann type (zero flux). A surface-based dipole-dipole survey is used with 47 electrodes spaced every 2 m, from $x = 4$ m to $x = 96$ m. To avoid artefacts associated with boundary conditions, a large buffer zone of 10 log-spaced nodes (~ 700 m) is added to the left and right model edges as well as to the bottom of the domain. For the forward computation, the mean value of the true field is used in this buffer zone. To mimic realistic measurement errors, heteroskedastic normally distributed noise

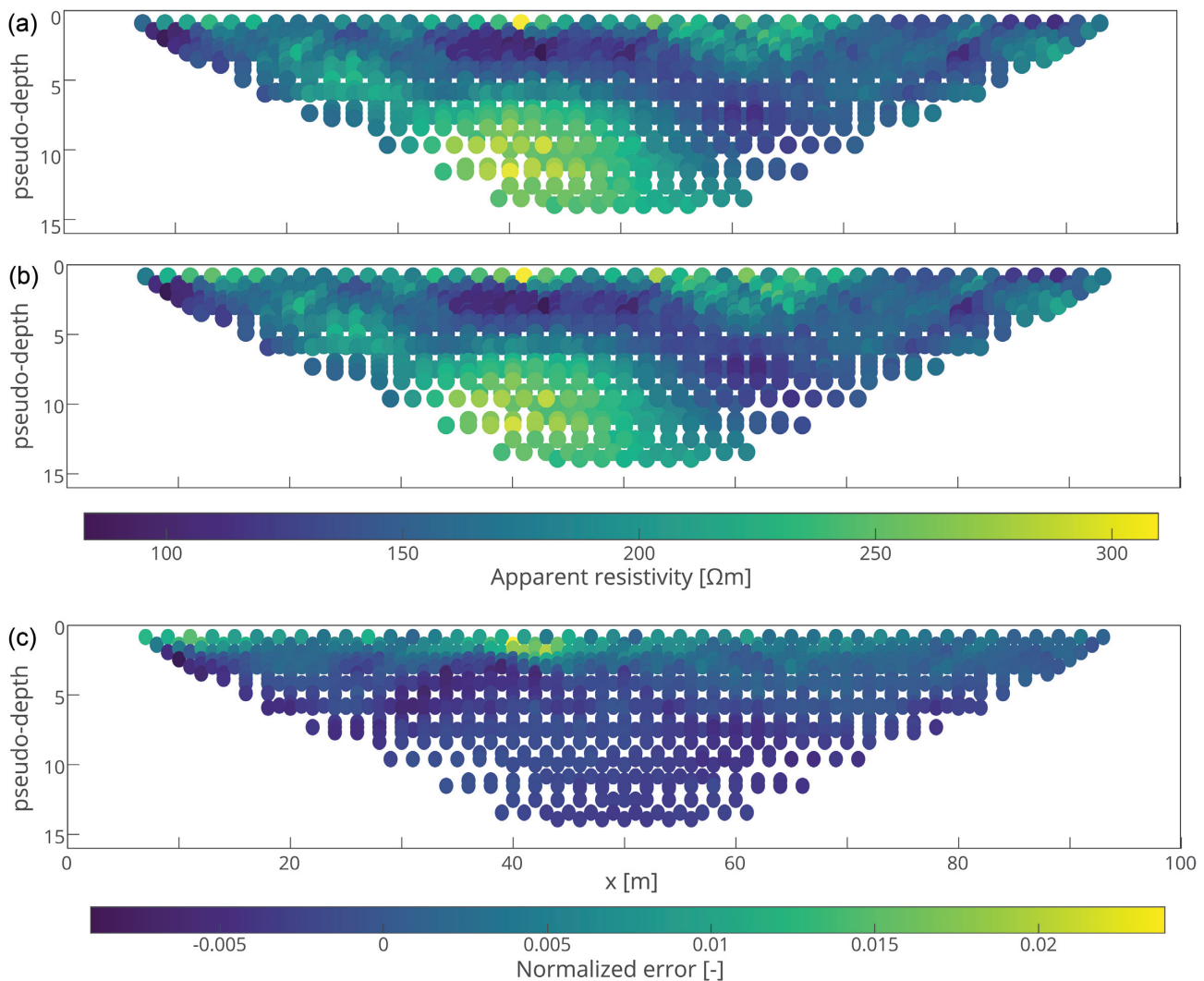


Figure 8. Comparison of the pseudo-sections of the apparent resistivity. (a) Observed apparent resistivity and (b) the mean forward response of 500 stochastic realizations, and (c) the normalized relative error of the realizations $(\bar{f}(\sigma_c^{\text{sim}}) - \mathbf{r}^{\text{obs}})/\mathbf{r}^{\text{obs}}$. The similarity between (a) and (b) highlights the ability of the method to reproduce the observation of the ERT survey. A normalized error up to 0.02 is expected due to the synthetic measurement errors that were added and accounted for in the inversion.

with a standard deviation s_ε is added to the simulated resistances to create the ‘observed’ data \mathbf{r}^{obs} . The inversion of the observed resistances is performed with the inversion subroutine of R2 (Binley & Kemna 2005) using the mean value of the apparent electrical conductivity as the initial model. The resolution of the inversion grid in the y -axis is log-spaced with thinner cells near the surface and larger ones in the bottom. This is common in geophysical inversion to tailor the grid resolution to the information content retrievable from a surface-based survey. To be consistent with the considered ratio of covariance ranges, the model regularization operator penalizes horizontal variations ten times more strongly than vertical variations.

Based on the output of R2 at the last iteration, the posterior covariance and the resolution matrix were computed using eqs (4) and (5). However, adaptations were necessary due to the buffer zone used during the inversion. Indeed, the rows and columns of the resolution matrix also include nodes corresponding to the buffer zone. Since the zone of interest does not include this buffer zone, the resolution matrix is split in two parts: \mathbf{R}_{in} for the columns of \mathbf{R} pertaining to model cells in the interior and \mathbf{R}_{out} for the columns

of \mathbf{R} pertaining to model cells in the buffer zone. The true field Σ^{true} related to the zone to be simulated does not include the buffer zone, whereas the known estimated tomogram Σ^{est} does. Thus, the contribution of the buffer zone $\mathbf{R}_{\text{out}}(i, :)$ is subtracted by the estimated tomogram in the buffer zone $\Sigma_{\text{out}}^{\text{est}}$ in order to remove its influence on the estimation process, such that,

$$\Sigma^{\text{est}}(i) - \mathbf{R}_{\text{out}}(i, :) \Sigma_{\text{out}}^{\text{est}} = \mathbf{R}_{\text{in}}(i, :) \Sigma^{\text{true}}. \quad (16)$$

Table 1 provides a summary of the parameters used to generate the synthetic electrical conductivity structure and the corresponding ERT-type geoelectric measurements.

3.2 Kriging estimation and simulation

The area-to-point kriging system is constructed following Section 2.3. In order to account for the presence of hard data, the kriging equations are updated as detailed in Appendix C. Fig. 4 shows the resulting area-to-point kriging estimation $\hat{\mathbf{z}}$ based on Σ^{est} and the conditioning data \mathbf{z}^{hd} .

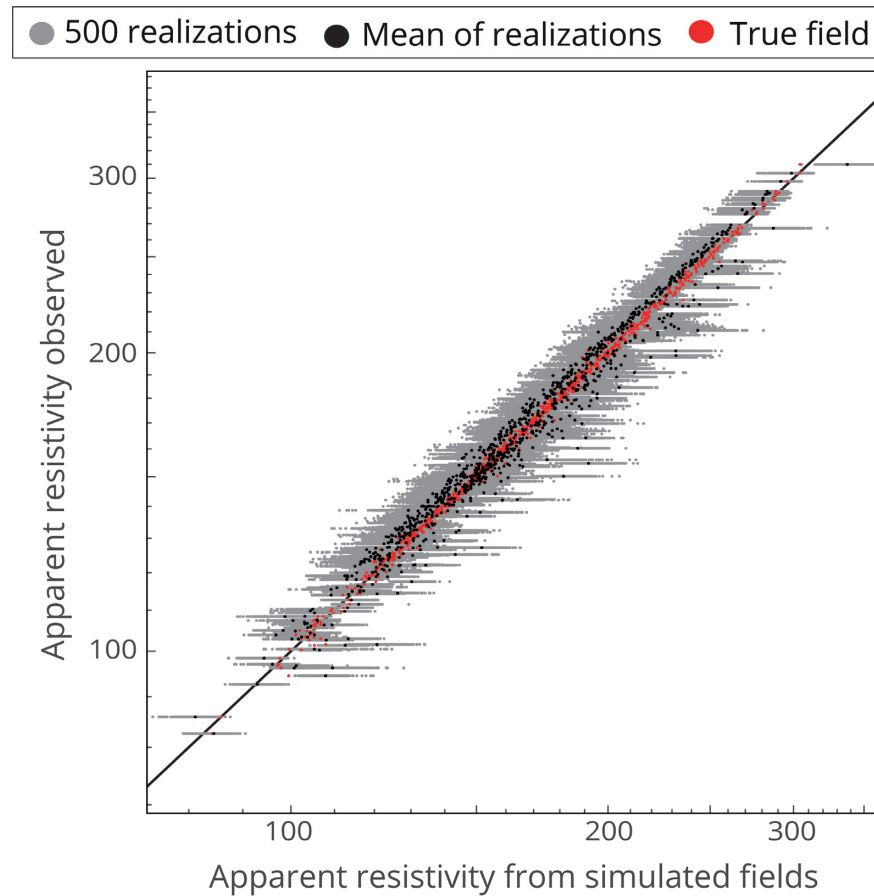


Figure 9. Comparison of the simulated and observed apparent resistivities for the 500 realizations. The high correlation (1:1 line) of the simulated and observed apparent resistivity shows the ability of the method to generate electrical resistivity fields coherent with the given tomogram. The small fluctuations with the true field (red) are due to the synthetic measurement errors added. The large variations with the realizations demonstrate the inability of the method to generate fields reproducing the apparent resistivity at the noise level.

From the kriging estimation $\hat{\mathbf{z}}$, stochastic realizations (i.e. simulation) $\mathbf{z}_c^{\text{sim}}$ can be produced using the Gaussian error simulation as detailed in Appendix D. Based on this workflow, 500 posterior realizations are generated to assess if the variability of fine-scale conductivity realizations is consistent with the tomogram and the underlying geostatistical model. Fig. 5 compares the normalized true field \mathbf{z}^{true} to a randomly selected conditional realization $\mathbf{z}_c^{\text{sim}}$, the mean of the 500 realizations $\bar{\mathbf{z}}_c^{\text{sim}}$ and the corresponding standard deviation $\text{std}(\mathbf{z}_c^{\text{sim}})$. Visual appraisal of the considered example realization (Fig. 5b) indicates that the stochastic simulations correctly reproduce the texture of \mathbf{z}^{true} , while the mean field (Fig. 5c) shows that the realizations capture the larger-scale features, with increasing details towards the surface and the borehole location, along which the hard data have been sampled. The mean field is very similar to Fig. 4(a), which is expected as the mean of the realizations tends towards the kriging estimation. The standard deviation field (Fig. 5d) shows that the realizations are less variable near the surface and near the borehole.

Fig. 6 compares the empirical probability density and semi-variogram of the 500 realizations with the true field \mathbf{z}^{true} and the underlying theoretical model, defined by a standard Gaussian distribution with covariance \mathbf{C}_z . These results confirm that, with some

ergodic fluctuations, the spatial statistics are reasonably well reproduced and the inclusion of the coarse tomogram did not induce a bias (Figs 6a and b). Empirical semi-variograms of the realizations show an adequate reproduction of the spatial structure of the theoretical model. However, as the spatial structure of the realizations is also influenced by the spatial information contained in the tomogram, and ultimately by the true field, the empirical variograms of the realizations appear to differ from the theoretical model in a similar manner as those of the true field.

Fig. 7 compares the RU-transform of the 500 conditional realizations (Figs 7b–d) to the inverted field \mathbf{Z}^{est} (Fig. 7a). Both the single upscaled realization (Fig. 7b) and the mean of the 500 realizations (Fig. 7c) present a good match to the inverted field (Fig. 7a). Although, a detailed analysis of the standard deviation of the RU-transform in Fig. 7(d) highlights some variability close to surface.

3.3 Corroboration with apparent resistivity data

When applying a two-step approach to a nonlinear problem, there is no guarantee that the resulting geostatistical realizations are fully compatible with the observed geophysical data (e.g. Bosch 2004).

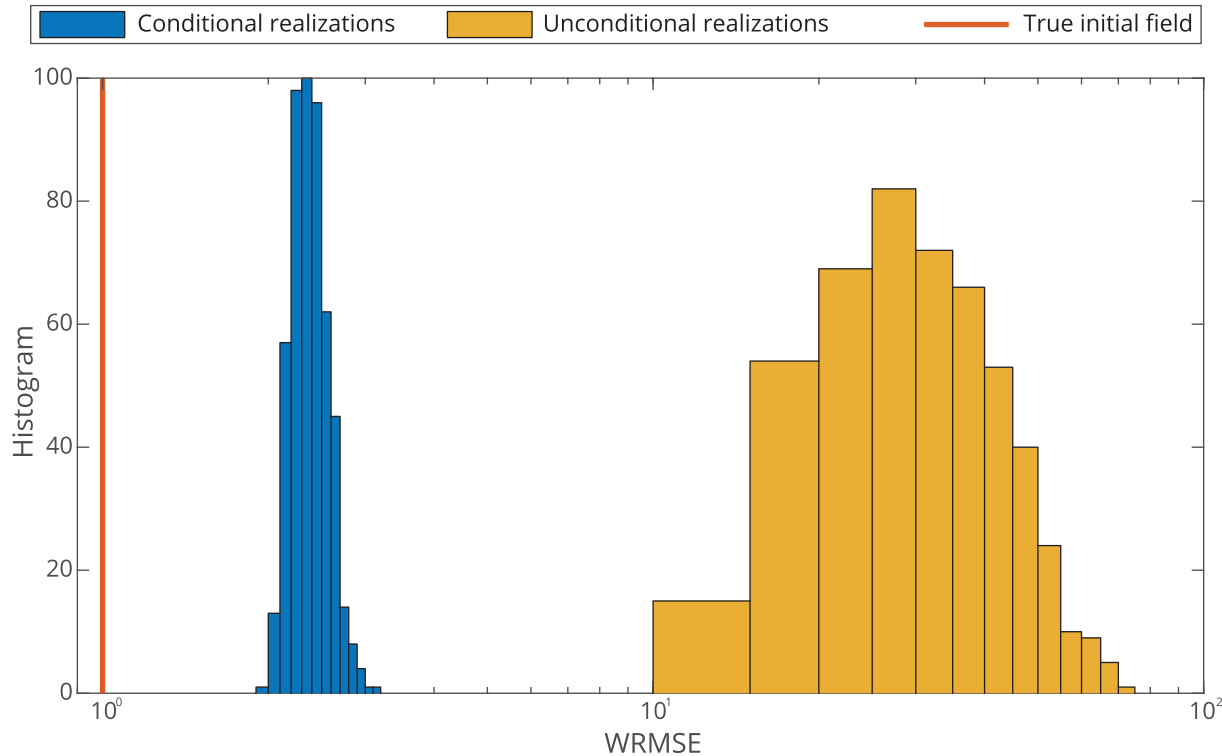


Figure 10. Histogram of the WRMSE misfit of 500 realizations. This figure illustrates the reduction of WRMSE with field generated by the method (blue) compared to unconditional simulation. However, there is still a gap between the noise level of the true field (red line) and the conditional realization.

Table 1. Summary of parameter values used for generating the electrical conductivity distribution and the corresponding ERT-type geoelectric measurements.

Name	Symbol	Value
Domain size (m)	$x_{\max} \times z_{\max}$	100×15
Fine-scale grid size	$n_x \times n_z$	500×30
Coarse-scale grid size (vertically log-spaced)	$n_x \times n_z$	100×15
Log mean porosity	μ_ϕ	-1.58
Porosity variance	s_ϕ^2	0.22
Covariance function	$C(\mathbf{h})$	exponential
Covariance range (m)	r_x, r_y	40×4
Electrical conductivity of pore water (mS m^{-1})	σ_w	43
Cementation exponent	m	1.4
Standard deviation of proportional error measurement	s_ε	0.02

One way to assess the information loss is to simulate the forward response from the various realizations and then to compare them with the observed data (Linde *et al.* 2015a).

Here, we calculate the forward response of our 500 geostatistical realizations. The pseudo-sections of the observed apparent resistivity (Fig. 8a) is overall well reproduced by the average simulated apparent resistivity of all 500 model realizations (Fig. 8b). The normalized error $(\bar{f}(\sigma_c^{\text{sim}}) - \mathbf{r}^{\text{obs}})/\mathbf{r}^{\text{obs}}$ (Fig. 8c) indicates some discrepancies, particularly near the surface. Some small discrepancies are expected as 2 per cent noise was added in the generation of the observed data. In Fig. 9, the effect of this added noise is highlighted

by the fact that the forward response of the true field (red dots) is not perfectly aligned with the 1:1 curve (corresponding to the observed apparent resistivities). Yet, the apparent resistivity response of the 500 realizations, as well as its mean, produce much larger variations than what can be explained by the added noise.

This data misfit can be quantified with the weighted root-mean square error (WRMSE),

$$\text{WRMSE} = \sqrt{\frac{1}{N} \sum_{i=1}^N \left(\frac{f(\sigma_c^{\text{sim}})_i - \mathbf{r}_i^{\text{obs}}}{s_\varepsilon \mathbf{r}_i^{\text{obs}}} \right)^2}. \quad (17)$$

Fig. 10 compares the WRMSE values of the forward response of conditional realizations generated by the proposed method against the true field and the unconditional realizations. Even if the conditional realizations perform much better than the unconditional ones, their mean WRMSE of 2.4 indicates that they are unable to produce residuals that are in agreement with the added noise (i.e. a WRMSE of 1). The origin of this information loss can be traced back to the difference between the inverted field \mathbf{Z}^{est} and the $\mathbf{R}\mathbf{U}$ -transform of the true field $\mathbf{R}\mathbf{U}\mathbf{z}^{\text{true}}$ (Fig. 3). Indeed, while the forward response of \mathbf{Z}^{est} produces correctly a WRMSE equal to one, the one of $\mathbf{R}\mathbf{U}\mathbf{z}^{\text{true}}$ is equal to 2.5. The first reason is that the forward response is affected by the upscaling. The forward response of the upscaled true field $\mathbf{U}\mathbf{z}^{\text{true}}$ has a WRMSE of 1.75; without upscaling, the forward response of the true field \mathbf{z}^{true} leads to a WRMSE of 0.98. The second reason is that the resolution matrix \mathbf{R} is based on a linearization around the final iteration. To investigate this effect, the Jacobian and posterior covariance matrix were computed directly based on the true model at the fine scale, such that the linearization is computed on the true fine-scale model. Here, the resulting WRMSE based on $\mathbf{R}^{\text{true}}\mathbf{z}^{\text{true}}$ is 1.53. By combining the error of these two

contributions $\sqrt{1.75^2 + 1.53^2} = 2.32$ leads to an error close to the error of 2.5 found in the model realizations.

4 DISCUSSION AND CONCLUSIONS

This study presents a two-step approach for producing fine-scale stochastic realizations of a rock physical property based on a corresponding geostatistical model and a low-resolution tomographic image resulting from a smoothness-constrained deterministic inversion of geophysical data. The stochastic realizations can be conditioned to pertinent hard data, such as, for example, geophysical borehole logs. The proposed technique relies on area-to-point kriging, which requires a linear support function between the targeted fine-scale structure and the coarse resolution of the tomogram. This is achieved through the model resolution and posterior covariance matrices computed for the tomographic image at the last iteration of a linearized inversion. The method was tested and verified with regard to a synthetic ERT-type case study for a strongly heterogeneous subsurface model. This choice was motivated by the widespread use of geoelectric measurements, the importance of electrical conductivity as a rock physical property, and the generally low and spatially variable resolution of the corresponding tomographic images. The results demonstrate that the proposed methodology is able to generate fine-scale electrical conductivity realizations that faithfully reproduce the two-point statistics of the underlying geostatistical model, while also being constrained to the large-scale structure defined by the tomogram. In this context, it is important to note that the proposed method can be applied to any type of tomographic image resulting from a least-squares-type of deterministic inversion that has been regularized based on smoothness or other regularization constraints, such as damping or curvature.

Arguably, the main advantage of the proposed method is its ability to provide posterior realizations at a low computational cost compared to more rigorous and/or comprehensive approaches, such as, for example, MCMC techniques. This is illustrated by the fact that for the synthetic case study considered in this work, the computational cost associated with an MCMC approach would have exceed that of the method presented in this study by two to three orders of magnitude. In the current implementation of our method, the computationally limiting factor is the size of the coarse-scale grid when solving the kriging system. This computational efficiency does, however, come at a price, as the proposed method is limited to scenarios where the fine-scale structure is multivariate Gaussian and its parameters (mean, variance and covariance) are known. While this is somewhat restrictive, it corresponds to a common assumption. These parameters are typically determined based on *a priori* knowledge, through trial-and-error, or inferred from complementary data, such as, for example, borehole logs. Finally, our method also requires the availability of the full resolution and the posterior covariance matrices.

The analysis of Section 3.3 reveals that although the realizations have the correct spatial statistics and match the coarse-scale tomogram when upscaled, they do not generate exactly the same forward response as the synthetic reference field. This is attributed to (1) the linear upscaling used to link the coarse and fine scales and (2) the linearization around the final inversion model for computing the resolution and posterior covariance matrices. While the latter point is inherent to deterministic least-squares-type inversion approaches, the first issue could be dealt with by using smaller mesh spacing for the coarse scale, which would sensibly increase the computational cost.

ACKNOWLEDGEMENTS

This work has been supported by a grant from the Swiss National Science Foundation. Comments and suggestions by the editor Ute Weckmann, Thomas Mejer Hansen, Odd Kolbjørnsen and an anonymous referee helped to improve the quality of this paper.

REFERENCES

- Alumbaugh, D.L. & Newman, G.A., 2000. Image appraisal for 2-D and 3-D electromagnetic inversion, *Geophysics*, **65**(5), 1455.
- Archie, G.E., 1942. The electrical resistivity log as an aid in determining some reservoir characteristics, *Trans. AIME*, **146**(01), 54–62.
- Atkinson, P.M., 2013. Downscaling in remote sensing, *Int. J. Appl. Earth Obs. Geoinf.*, **22**(1), 106–114.
- Binley, A. & Kemna, A., 2005. DC resistivity and induced polarization methods, in *Hydrogeophysics*, Vol. **50**, pp. 129–156, eds Rubin, Y. & Hubbard, S.S., Springer Netherlands.
- Bosch, M., 2004. The optimization approach to lithological tomography: combining seismic data and petrophysics for porosity prediction, *Geophysics*, **69**(5), 1272–1282.
- Cassiani, G., Böhm, G., Vesnauer, A. & Nicolich, R., 1998. A geostatistical framework for incorporating seismic tomography auxiliary data into hydraulic conductivity estimation, *J. Hydrol.*, **206**(1–2), 58–74.
- Chen, J., Hubbard, S. & Rubin, Y., 2001. Estimating the hydraulic conductivity at the South Oyster Site from geophysical tomographic data using Bayesian techniques based on the normal linear regression model, *Water Resour. Res.*, **37**(6), 1603–1613.
- Constable, S.C., Parker, R.L. & Constable, C.G., 1987. Occam's inversion: a practical algorithm for generating smooth models from electromagnetic sounding data, *Geophysics*, **52**(3), 289–300.
- Cpty, N., Rubin, Y. & Mavko, G., 1993. Geophysical-hydrological identification of field permeabilities through Bayesian updating, *Water Resour. Res.*, **29**(8), 2813–2825.
- Day-Lewis, F.D. & Lane, J.W., 2004. Assessing the resolution-dependent utility of tomograms for geostatistics, *Geophys. Res. Lett.*, **31**(7).
- DeGroot-Hedlin, C. & Constable, S., 1990. Occam's inversion to generate smooth, two-dimensional models from magnetotelluric data, *Geophysics*, **55**(12), 1613–1624.
- Dentz, M., Le Borgne, T., Englert, A. & Bijeljic, B., 2011. Mixing, spreading and reaction in heterogeneous media: a brief review, *J. Contam. Hydrol.*, **120–121**(C), 1–17.
- Doyen, P.M. & Boer, L.D., 1996. Bayesian sequential Gaussian simulation of lithology with non-linear data, US Patent 5539704.
- Englert, A., Kemna, A., Zhu, J., Vanderborght, J., Vereecken, H. & Yeh, T.-C.J., 2016. Comparison of smoothness-constrained and geostatistically based cross-borehole electrical resistivity tomography for characterization of solute tracer plumes, *Water Sci. Eng.*, **9**(4), 274–286.
- Friedel, S., 2003. Resolution, stability and efficiency of resistivity tomography estimated from a generalized inverse approach, *Geophys. J. Int.*, **153**(2), 305–316.
- Gloaguen, E., Marcotte, D. & Chouteau, M., 2004. A non-linear GPR tomographic inversion algorithm based on iterated cokriging and conditional simulations, in *Geostatistics Banff 2004*, pp. 409–418, eds Leuangthong, O. & Deutsch, C.V., Springer Netherlands.
- Gloaguen, E., Marcotte, D., Chouteau, M. & Perroud, H., 2005. Borehole radar velocity inversion using cokriging and cosimulation, *J. Appl. Geophys.*, **57**(4), 242–259.
- Gloaguen, E., Marcotte, D., Giroux, B., Dubreuil-Boisclair, C., Chouteau, M. & Aubertin, M., 2007. Stochastic borehole radar velocity and attenuation tomographies using cokriging and cosimulation, *J. Appl. Geophys.*, **62**(2), 141–157.
- Gotway, C.A. & Young, L.J., 2002. Combining incompatible spatial data, *J. Am. Stat. Assoc.*, **97**(458), 632–648.
- Hansen, T.M. & Mosegaard, K., 2008. VISIM: sequential simulation for linear inverse problems, *Comput. Geosci.*, **34**(1), 53–76.

- Hansen, T.M., Journel, A.G., Tarantola, A. & Mosegaard, K., 2006. Linear inverse Gaussian theory and geostatistics, *Geophysics*, **71**(6), R101–R111.
- Hansen, T.M., Cordua, K.S. & Mosegaard, K., 2012. Inverse problems with non-trivial priors: efficient solution through sequential Gibbs sampling, *Comput. Geosci.*, **16**(3), 593–611.
- Hoeksema, R.J. & Kitanidis, P.K., 1984. An application of the geostatistical approach to the inverse problem in two-dimensional groundwater modeling, *Water Resour. Res.*, **20**(7), 1003–1020.
- Hubbard, S.S. et al., 2001. Hydrogeological characterization of the south oyster bacterial transport site using geophysical data, *Water Resour. Res.*, **37**(10), 2431–2456.
- Journel, A.G. & Huijbregts, C.J., 1978. *Mining Geostatistics*, Academic Press.
- Kitanidis, P.K., 1995. Quasi-linear geostatistical theory for inversing, *Water Resour. Res.*, **31**(10), 2411–2419.
- Kitanidis, P.K. & Vomvoris, E.G., 1983. A geostatistical approach to the inverse problem in groundwater modeling (steady state) and one-dimensional simulations, *Water Resour. Res.*, **19**(3), 677–690.
- Kyriakidis, P.C., 2004. A geostatistical framework for area-to-point spatial interpolation, *Geogr. Anal.*, **36**(3), 259–289.
- Kyriakidis, P.C. & Yoo, E.H., 2005. Geostatistical prediction and simulation of point values from areal data, *Geogr. Anal.*, **37**(2), 124–151.
- Le Ravalec-Dupin, M., Noettinger, B. & Hu, L.Y., 2000. The FFT moving average (FFT-MA) generator: an efficient numerical method for generating and conditioning Gaussian simulations, *Math. Geol.*, **32**(6), 701–723.
- Li, W., Nowak, W. & Cirpka, O.A., 2005. Geostatistical inverse modeling of transient pumping tests using temporal moments of drawdown, *Water Resour. Res.*, **41**(8), 1–13.
- Linde, N., Binley, A., Tryggvason, A., Pedersen, L.B. & Revil, A., 2006. Improved hydrogeophysical characterization using joint inversion of cross-hole electrical resistance and ground-penetrating radar traveltimes, *Water Resour. Res.*, **42**(12), 1–16.
- Linde, N., Lochbühler, T., Dogan, M. & Van Dam, R.L., 2015a. Tomogram-based comparison of geostatistical models: application to the Macrodispersion Experiment (MADE) site, *J. Hydrol.*, **531**, 543–556.
- Linde, N., Renard, P., Mukerji, T. & Caers, J., 2015b. Geological realism in hydrogeological and geophysical inverse modeling: a review, *Adv. Water Res.*, **86**, 86–101.
- Mariethoz, G., Renard, P. & Froidevaux, R., 2009. Integrating collocated auxiliary parameters in geostatistical simulations using joint probability distributions and probability aggregation, *Water Resour. Res.*, **45**(8).
- McKenna, S.A. & Poeter, E.P., 1995. Field example of data fusion in site characterization, *Water Resour. Res.*, **31**(12), 3229–3240.
- Menke, W., 1989. *Geophysical Data Analysis: Discrete Inverse Theory*, Vol. 45, Academic Press.
- Moysey, S. & Knight, R., 2004. Modeling the field-scale relationship between dielectric constant and water content in heterogeneous systems, *Water Resour. Res.*, **40**(3), 1–10.
- Moysey, S., Singha, K. & Knight, R., 2005. A framework for inferring field-scale rock physics relationships through numerical simulation, *Geophys. Res. Lett.*, **32**(8), 1–4.
- Newman, G.A. & Alumbaugh, D.L., 2000. Three-dimensional magnetotelluric inversion using non-linear conjugate gradients, *Geophys. J. Int.*, **140**(2), 410–424.
- Pirot, G., Linde, N., Mariethoz, G. & Bradford, J.H., 2017. Probabilistic inversion with graph cuts: application to the Boise Hydrogeophysical Research Site, *Water Resour. Res.*, **53**(2), 1231–1250.
- Ramirez, A.L. et al., 2005. Stochastic inversion of electrical resistivity changes using a Markov Chain Monte Carlo approach, *J. geophys. Res.*, **110**(B2), 1–18.
- Rubin, Y., Mavko, G. & Harris, J., 1992. Mapping permeability in heterogeneous aquifers using hydrologic and seismic data, *Water Resour. Res.*, **28**(7), 1809–1816.
- Ruggeri, P., Irving, J., Gloaguen, E. & Holliger, K., 2013. Regional-scale integration of multiresolution hydrological and geophysical data using a two-step Bayesian sequential simulation approach, *Geophys. J. Int.*, **194**(1), 289–303.
- Ruggeri, P., Gloaguen, E., Lefebvre, R., Irving, J. & Holliger, K., 2014. Integration of hydrological and geophysical data beyond the local scale: application of Bayesian sequential simulation to field data from the Saint-Lambert-de-Lauzon site, Québec, Canada, *J. Hydrol.*, **514**, 271–280.
- Singha, K., Day-Lewis, F.D. & Moysey, S., 2007. Accounting for tomographic resolution in estimating hydrologic properties from geophysical data, in *Subsurface Hydrology: Data Integration for Properties and Processes*, pp. 227–241, American Geophysical Union.
- Tarantola, A. & Valette, B., 1982. Generalized nonlinear inverse problems solved using the least squares criterion, *Rev. Geophys.*, **20**(2), 219–232.
- Yeh, T.-C.J., Liu, S., Glass, R.J., Baker, K., Brainard, J.R., Alumbaugh, D.L. & LaBrecque, D., 2002. A geostatistically based inverse model for electrical resistivity surveys and its applications to vadose zone hydrology, *Water Resour. Res.*, **38**(12), 14–11–14–13.

APPENDIX A: LINEAR MAPPING

The use of the area-to-point framework requires the fine-scale and coarse-scale variables to be linearly related. This appendix provides the mathematical demonstration for eq. (10). This is shown by combining eqs (1), (3), (6) and (7) into

$$\mathbf{Z}^{\text{est}} = \frac{\Sigma^{\text{est}} - \mu_{\sigma}}{s_{\sigma}} = \frac{\mathbf{R}\Sigma^{\text{true}} - \mu_{\sigma}}{s_{\sigma}} = \frac{\mathbf{R}\mathbf{U}\sigma^{\text{true}} - \mu_{\sigma}}{s_{\sigma}}. \quad (\text{A1})$$

Since $\mathbf{R}\mathbf{U}$ is an operator with all sums of rows equal to one, applying it to a vector of equal values does not affect this vector, such that $\mu_{\sigma} = \mathbf{R}\mathbf{U}\mu_{\sigma}$. Thus eq. (A1) becomes

$$\mathbf{Z}^{\text{est}} = \frac{\mathbf{R}\mathbf{U}\sigma^{\text{true}} - \mathbf{R}\mathbf{U}\mu_{\sigma}}{s_{\sigma}} = \mathbf{R}\mathbf{U}\frac{\sigma^{\text{true}} - \mu_{\sigma}}{s_{\sigma}} = \mathbf{R}\mathbf{U}\mathbf{z}^{\text{true}}. \quad (\text{A2})$$

APPENDIX B: ACCOUNTING FOR DATA ERROR AND REGULARIZATION IN THE COVARIANCE \mathbf{C}_Z

We demonstrate below how to update the covariance matrix of \mathbf{Z} to account for the effects of the data errors and the regularization term used in the inversions. Indeed, the inverted tomogram Σ^{est} contains additional correlation in their data due to the regularization and uncertainty of the measurement. These effects are accounted for by the covariance $\mathbf{C}_{\Sigma}^{\text{est}}$ of eq. (5). The covariance matrix $\mathbf{C}_{Z'}$ used to compute the kriging weights in eq. (9) is thus the addition of the spatial structure \mathbf{C}_Z and $\mathbf{C}_{\Sigma}^{\text{est}}$,

$$\mathbf{C}_{Z'} = \mathbf{C}_Z + \left(\frac{1}{s_{\sigma}} \right)^2 \mathbf{C}_{\Sigma}^{\text{est}}. \quad (\text{B1})$$

The diagonal of the covariance matrices \mathbf{C}_Z and $\mathbf{C}_{\Sigma}^{\text{est}}$ is displayed in Fig. B1. The difference in magnitude points to the relatively small importance of the error estimates of the tomogram compared to the variability of the geostatistical model. Note that values above one are possible because the top rows of \mathbf{Z} have smaller grid sizes than \mathbf{z} , thus increasing the variance.

APPENDIX C: AREA-TO-POINT KRIGING WITH POINT CONDITIONING

The area-to-point kriging eqs (8) and (9) can be modified to account for the presence of known error-free hard data \mathbf{z}^{hd} . The contribution of \mathbf{z}^{hd} in the kriging estimate is simply added to eq. (8) with the kriging weights Λ_{hd} ,

$$\hat{\mathbf{z}} = \Lambda_{\text{hd}}\mathbf{z}^{\text{hd}} + \Lambda\mathbf{Z}^{\text{est}}, \quad (\text{C1})$$

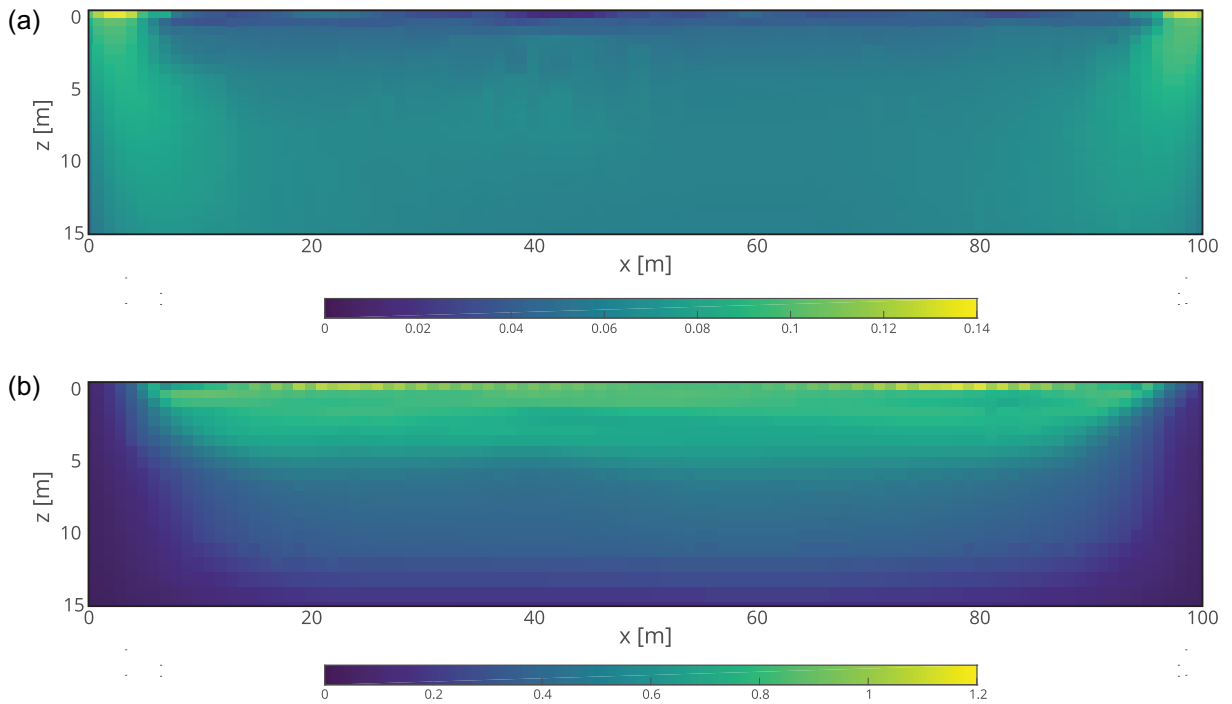


Figure B1. Diagonals of the covariance matrices (a) resulting from the inversion $(\frac{1}{s_\sigma})^2 \mathbf{C}_\Sigma^{\text{est}}$ and (b) of the geostatistical model \mathbf{C}_Z . The relative magnitude of these figures shows the smaller influence of the covariance matrix resulting from the inversion compared to the geostatistical model. The variability of the geostatistical model with depth is due to the change of grid size, thus also explaining a variance above one for the top cell.

and the kriging system is updated to

$$\begin{bmatrix} \mathbf{C}_Z & \mathbf{C}_{Z, z^{\text{hd}}} \\ \mathbf{C}_{z^{\text{hd}}, Z} & \mathbf{C}_{z^{\text{hd}}} \end{bmatrix} \begin{bmatrix} \boldsymbol{\Lambda} \\ \boldsymbol{\Lambda}_{\text{hd}} \end{bmatrix} = \begin{bmatrix} \mathbf{C}_{\hat{z}, Z} \\ \mathbf{C}_{\hat{z}, z^{\text{hd}}} \end{bmatrix}. \quad (\text{C2})$$

This linear system is solved simultaneously for $\boldsymbol{\Lambda}$ and $\boldsymbol{\Lambda}_{\text{hd}}$.

APPENDIX D: AREA-TO-POINT CONDITIONAL SIMULATION

Gaussian error simulation is used to generate the conditional simulations $\mathbf{z}_c^{\text{sim}}$. The procedure is briefly recalled below for a single simulation and more thoroughly described in Kyriakidis & Yoo (2005) for the general case of area-to-point kriging.

(1) Construct an unconditional simulation \mathbf{z}^{sim} , for instance, using the FFT-MA method (Le Ravalec-Dupin *et al.* 2000):

$$\mathbf{z}^{\text{sim}} \leftarrow \mathcal{N}(0, \mathbf{C}_z). \quad (\text{D1})$$

(2) Compute the corresponding RU-transform of \mathbf{z}^{sim} , denoted as \mathbf{Z}^{sim} :

$$\mathbf{Z}^{\text{sim}} = \mathbf{R}\mathbf{U}\mathbf{z}^{\text{sim}}. \quad (\text{D2})$$

(3) Compute the area-to-point kriging estimate of the unconditional simulation $\hat{\mathbf{z}}^{\text{sim}}$. The hard data to be used are sampled in \mathbf{z}^{sim} at the same locations than \mathbf{z}^{hd} . This location is denoted \mathbf{u}^{hd} , such as $\mathbf{z}^{\text{hd}} = \mathbf{z}^{\text{true}}(\mathbf{u}^{\text{hd}})$. The area-to-point kriging estimate is

$$\hat{\mathbf{z}}^{\text{sim}} = \boldsymbol{\Lambda}_z \mathbf{z}^{\text{sim}}(\mathbf{u}^{\text{hd}}) + \boldsymbol{\Lambda}_Z \mathbf{Z}^{\text{sim}}. \quad (\text{D3})$$

(4) Compute the conditional simulation $\mathbf{z}_c^{\text{sim}}$ based on \mathbf{z}^{sim} , $\hat{\mathbf{z}}^{\text{sim}}$ and the area-to-point kriging (eq. 8):

$$\mathbf{z}_c^{\text{sim}} = \hat{\mathbf{z}} + [\mathbf{z}^{\text{sim}} - \hat{\mathbf{z}}^{\text{sim}}]. \quad (\text{D4})$$